Two-dimensional RMHD modeling assessment of current flow, plasma conditions, and Doppler effects in recent Z argon experiments

J. W. Thornhill, J. L. Giuliani, *Member, IEEE,* B. Jones, *Member, IEEE,* J. P. Apruzese, A. Dasgupta, *Member, IEEE,* Y. K. Chong, *Member, IEEE,* A. J. Harvey-Thompson, D. J. Ampleford, S. B. Hansen, C. A. Coverdale, *Fellow, IEEE,* C. A. Jennings, G. A. Rochau, M. E. Cuneo, *Senior Member, IEEE*, D. C. Lamppa, D. Johnson, M.C. Jones, N. W. Moore, E. M. Waisman, M. Krishnan, and P. L. Coleman

Abstract— In order to determine current-loss circuit parameters, the Mach2-TCRE two-dimensional radiation magnetohydrodynamic (2DMHD) model was benchmarked against the radiative and electrical properties of three recent argon gas-puff experiments (same initial conditions) performed on the Z machine at Sandia National Laboratories. The model indicates that there were current losses occurring near or within the diode region of the Z machine during the stagnation phase of the implosion. The "best" simulation reproduces the experimental K-shell powers, K-shell yields, total powers, percentage of emission radiated in α lines, size of the K-shell emission region, and the average electron temperature near the time of peak K-shell power. The calculated atomic populations, ion temperatures, and radial velocities are used as input to a detailed multi-frequency ray-trace radiation transport model that includes the Doppler effect. This model is employed to construct time-, space-, and energy- resolved synthetic spectra. The role the Doppler effect is likely playing in the experiments is demonstrated by comparing synthetic spectra generated with and without this effect.

Index Terms—K-shell radiation, collisional radiative equilibrium, Doppler effects

I. INTRODUCTION

A series of three 8 cm diameter nozzle argon gas-puff experiments were recently performed on the Z machine

at Sandia National Laboratories [1]. All the experiments had the same initial density profile, load mass of 1 mg/cm and length of 2.5 cm. Given the uncertainty and unstable behavior that had been present in earlier argon pinch experiments on Z [2], it is notable that all three experiments produced nearly the same K-shell radiative power pulse and large > 300 kJ K-yield.

The reproducible radiative properties of the experiments imply that the coupling of energy from the machine to the gas-puff loads was consistent and reliable, even though it may not be fully understood. These well-diagnosed experiments also enabled us to benchmark and investigate the experiments using a multi-dimensional radiation MHD model.

In this investigation the two-dimensional radiation-magnetohydrodynamic (2DRMHD) code Mach2-TCRE [3] was benchmarked to the measured current and radiative properties of the experiments in order to determine current-loss circuit parameters. The benchmark simulations indicate that there were current losses downstream of the post-hole convolute near or within the pinch diode. Simulations performed with the benchmarked current-loss circuit parameters with load masses greater than the 1 mg/cm used in the experiments indicate that it would be beneficial to perform experiments at a larger mass to better understand the nature of this apparent current loss while possibly achieving higher K-yields.

The "best" simulation for the three experiments well reproduces: the experimental K-powers and yields; total powers; percent of K-shell radiation radiated in the α lines; size of the K-shell emission region; as well as the temperature of the pinch near the time of peak K-shell power as determined by the slope of the time integrated 4.4 – 5.0 keV free-bound continuum spectrum. The good match between simulated and experimental plasma radiative properties makes it worth examining the dynamic state (ion and electron temperatures and densities) of the simulated plasma near the time of peak K-shell power to infer the state of the experimental plasmas.

The "best" simulation results were post-processed with a radiation transport model that includes Doppler effects. This Doppler analysis shows that the velocity gradients in these simulations of the experimental argon gas-puff plasmas are

sufficient near the time of peak K-shell emission to produce: broadened line profiles; spectral energy shifts; and diminished line center self-absorption features – features that would otherwise be present in the absence of Doppler motion due to the large optical depth at the line center energy. Time-, space-, and energy-resolved spectra near the time of peak K-shell emission are generated that show a significant blue shift in the Ly-α spectrum just prior to the time of peak K-shell emission.

The next section (II) reviews the Mach2-TCRE 2DRMHD model including an improved calculation for escape probabilities, which are required as input to the TCRE equation of state tables. The process of benchmarking the model to the experiments is then described. Section (III) presents a comparison between simulated and experimental pinch radiative properties. Although some specific experimental information is shown here for the purpose of comparing to calculated results, the reader is referred to [1] for more detailed experimental information. In Section (IV) non-LTE aspects of the modeling and experiments are discussed and a post-process Doppler radiation transport calculation is described and used to generate synthetic time-dependent and spatially-integrated Ar He-α intensities near the time of peak K-shell emission. It is also used to generate synthetic time-, space-, and energy-resolved spectra. Results are summarized in the conclusion section (V).

II. Mach2-tcre modeling and benchmarking to experiments

A. The Mach2-TCRE Model

The two-dimensional magneto-hydrodynamics (2DMHD) code, Mach2 [4] is employed to model the multi-dimensional plasma motions that are present in gas-puff implosions. It is an arbitrary Lagrangian-Eulerian (ALE) resistive MHD simulation code with three components of velocity and magnetic field but only two spatial dimensions. In this investigation the calculations are performed in cylindrical geometry with azimuthal symmetry, azimuthal magnetic field, and in-plane (*r,z*) velocities. In order to increase grid resolution, especially near the time when most of the K-shell photons are emitted, a radially moving adaptive grid is implemented. This grid moves in a quasi-Lagrangian fashion such that the original radial grid that was uniformly distributed over 5.0 cm radius is compressed to a nearly uniform distribution over ~2.0 cm radius by the time stagnation occurs. There are 128 radial and 128 axial grid points used in the calculations.

To account for the non-LTE kinetics, opacity, and non-local transport of radiation that affect the atomic populations of these high temperature K-shell emitting argon plasmas, we incorporated into the Mach2 code a self-consistent equation of state calculation that models this physics. It is called the tabular collisional radiative equilibrium (TCRE) model [3]. The TCRE model is a computationally efficient and reasonably accurate method for modeling the non-LTE ionization dynamics and radiation transport of K-shell emitting multi-dimensional Z-pinch plasmas. The radiation source function for the model is obtained from a self-consistent CRE calculation for the atomic level populations.

All atomic structure and collisional and radiative data were calculated using the Flexible Atomic Code (FAC) suite of codes, see [5] Accurate line opacities and radiation transport are employed, and optically thin radiation is allowed to freely escape rather than diffuse.

The TCRE model uses a table look-up method that updates each zone's equation of state information based on knowledge of the plasma's electron internal energy, ion temperature, ion density, and the escape probabilities P_{esc} (as treated by Apruzese [6]-[8]) of pre-selected radiating lines, one from each ionization stage of argon. Each line is chosen such that it will be a good representative radiator when the plasma has an effective charge that is near that of the respective ionization stage from which the line radiates. For example, the Ar He-α line is a good choice for a representative line for the He-like stage of argon. The calculated P_{esc} for this line for a specific zone is defined here by,

$$P_{esc} = \frac{A - B - C}{A} \qquad (1)$$

where A is the number/sec-cm^3 of locally emitted Ar He-α photons, B is the number/sec-cm^3 of locally emitted Ar He-α photons that are absorbed locally, and C is the number/sec-cm^3 of non-local Ar He-α photons that are absorbed locally. The non-local radiation term C is calculated using a discrete ordinates approach for the transport of each dominant emission line in 3D throughout the whole plasma. Specifically the EQ$_4$ set [9] is used with 24 rays projected from each zone. Note that these rays are not coordinate-aligned to avoid biasing along the longest and shortest paths to escape. The ray trace radiation transport calculation couples the Ar He-α radiation from the other zones in the multi-dimensional plasma to the zone of interest as a function of the tabulated Ar He-α line center absorption coefficients.

In the past, the radiation coupling that occurs between remote plasma regions was simplified by use of the "on-the-spot (OTS) approximation" for P_{esc} – "*if a photon is emitted from a local region and it is absorbed anywhere in the plasma, then it is assumed to be absorbed in the emitting zone* [10]." In the simulations presented here the OTS simplification is not used. Instead, we adhere to the more physical definition of P_{esc} shown in formula (1) and calculate term C using the EQ$_n$ ray traced based radiation transport methodology developed by Apruzese *et al*. [11]. Unlike the OTS approximation, with this model, we self-consistently model both absorption and emission of photons into and out of each computational zone.

B. Initial Density and Current models for Simulations

The initial density profile for the argon gas puff load that is used as input to Mach2-TCRE is taken from the measured (high resolution interferometry) distribution of the 1: 1.6 gas-puff configuration. The details of the nozzle system are described by Krishnan [12] and the high resolution imaging interferometer is described by Coleman *et al*. [13] and an overview of the entire experimental setup is presented by Jones *et al*. [14]. The Sandia 8 cm diameter cylindrical nozzle has gas ejected from an inner annular region between 1 cm

and 2 cm radius and an outer annular region between 3 cm and 4 cm. The ratio 1:1.6 represents the relative mass load in each of these annular regions (outer:inner). Because of the noise in the interferometry measurements the distribution was "smoothed" by averaging over nearest neighbor data points 15 successive times,

$$\rho_{i,j}^{k+1} = \frac{\rho_{i,j}^k + \rho_{i+1,j}^k + \rho_{i-1,j}^k + \rho_{i,j+1}^k + \rho_{i,j-1}^k}{5} \qquad (2)$$

where k is the averaging step, i is the radial coordinate index, and j is the axial coordinate index. The $\rho_{i,j}$ are zone-centered values of the mass density ρ. This procedure is similar to that employed in an earlier argon gas-puff assessment for the Z machine [15]. The sensitivity of the simulated radiative properties of argon gas puff loads to this "smoothing" procedure are also discussed in [15].

Fig. 1 displays the measured currents in the MITL as well as in the feed section of the Z machine [16]. The yellow envelope shown in this figure encompasses the MITL currents and the grey envelope encompasses the feed currents. One can see from the range of measured feed currents that there is substantial shot-to-shot uncertainty in the amount of current that flows downstream of the post-hole convolute. There is even more uncertainty in the energy that ultimately gets coupled from the machine to the load because this energy scales with current squared.

A circuit model that represents the flow of current from the pulsed power machine to the load is required to implode the gas-puff load in the simulations. To our knowledge, there is no equivalent circuit model that presently can accurately predict the energy coupling from the Z machine into a gas-puff load. For this reason, the framework for circuit modeling that was outlined in Jennings *et al.* [17] was applied to posit the current flow into the experimental gas-puff loads. A time-dependent resistive circuit element, $R_{feed}(t)$, for modeling current losses downstream from the post-hole convolute (closer to or within the load region) of the machine is part of this framework, see Fig. 2. In this figure I_{MITL} is measured in the magnetically insulated transmission line (MITL) region of the machine, I_{Feed} is measured just downstream of the post-hole convolute and I_{load}, the current that implodes the gas-puff plasma, is not measured. $R_{MITL}(t)$ represents time-dependent resistive current losses in the MITL region.

Early on, when there are no current losses present, R_{MITL} and R_{feed} are set to a large non-conductive value of 5 Ohms, and later in time, when the losses are modeled to occur, the resistance is dropped precipitously, with a 4 ns decay time, to a much lower value, which can conduct current. For example,

$$R_{MITL}(t < t_M) = 5 \ Ohms \qquad (3)$$

$$R_{MITL}(t \geq t_M) = R_{MITL}(\infty) \\ + \left(5 \ Ohms - R_{MITL}(\infty)\right)e^{\frac{t_M-t}{4 \ ns}}$$

t_M is the turn-on time for current loss initiation and the asymptotic resistance value is $R_{MITL}(\infty)$. R_{feed} has a similar form but may have a different turn-on time t_F and asymptotic value $R_{feed}(\infty)$. The turn-on times and asymptotic resistance values that best represent the power flow that occurred in the experiments were not known apriori. For this reason,

numerous 2DRMHD simulations in which these parameters were varied were performed in order to find values that provided a "best" match to both the experimental electrical and radiative properties of the experiments.

In the work presented here, only two of the numerous Mach2-TCRE simulations performed to determine current-loss circuit parameters are discussed. They are labeled *A* and *B* and their calculated MITL and feed currents as well as the Z machine drive voltage $V_{eq}(t)$ are shown in Fig. 3. The turn-on times t_M and t_F for circuit *A* are both 110 ns, $R_{MITL}(\infty) = 0.2$ Ohms and $R_{feed}(\infty) = 0.3$ Ohms. For circuit *B*, t_M is 105 ns and $R_{MITL}(\infty)$ is 0.3 Ohms. R_{feed} is not modeled for circuit *B*. Circuit *A* has the "best" overall fit to both electrical and radiative properties (radiative properties to be described later). The calculated circuit *A* MITL current is reasonably close to the measured MITL currents and the calculated feed current lies near the middle of the gray envelope encompassing the measured feed currents. Circuit *B* results are discussed because there is uncertainty whether current losses downstream of the post-hole convolute really exist – they were not modeled prior to the work cited in [17]. The current flowing through the gas-puff load is the same as that flowing through the feed section when current losses downstream of the post-hole convolute are not modeled. Under this condition, one is forced to model a feed current that lies very close to the bottom of the grey envelope shown in Figs. 1 and 3. Otherwise, if one attempts to model a current larger than this, then the corresponding calculated MITL current will be even lower than is illustrated in Fig. 3, which is already well below the envelope of measured MITL currents.

III.   COMPARISON OF EXPERIMENTAL AND CALCULATED RADIATIVE PROPERTIES

In the comparison of simulations with the experimental data we reiterate that seven observed properties, including circuit and radiation data, were used to constrain the "best" fit: (i) the initial Ar density profile for the 1:1.6 distribution; (ii) the measured MITL and feed currents (see Fig.1); (iii) the electron temperature based on the slope of time integrated K-shell free-bound continuum between 4.4 keV and 5 keV (T_e = 1.8 keV-2.1 keV); (iv) the ratio of the sum of the He-like and H-like line emission to the total K-shell yield (ratio~80%); (v) the K-shell yield (three shot average ~330 kJ +/- 9%); (vi) the pulse shape of the K-shell power (peak power was 28 TW +/-10%); and (vii) the pulse shape of the total power (peak was 40 TW +/- 20%). Again, with the exception of the MITL and feed current information, these constraints were taken from reference [1].

The initial density profile was discussed in the previous section and the MITL and feed current results for models *A* and *B* were shown in Fig. 3. The electron temperature from the free-bound radiation was calculated by weighting the electron temperature of each zone by its high energy > 3 keV continuum K-shell power and then integrating in space over the volume of the pinch and integrating in time from -10 ns to +10 ns, where t=0 ns corresponds to the time of peak K-shell power. This result is then normalized by the total high energy continuum K-shell energy emitted during this 20 ns time

duration. Following this procedure the average temperature of the K-shell emission region was 1855 eV and 2970 eV, for simulation *A* and *B*, respectively. - the latter likely being significantly greater than the measured value range of 1.8 keV – 2.1 keV because of too large a load current. For the ratio of the K-shell lines to the total K-shell yield, simulations *A* and *B* gave 75% and 78%, respectively – both in agreement with the data.

The experimental and calculated K-shell yield and power as a function of time from t = - 20 ns to t = +20 ns are compared in Fig. 4. All three experiments produced total and K-shell power profiles that were nearly the same [1]. The average yield was 330 kJ with a shot-to-shot variation of +/- 9% and individual shot uncertainty of +/- 8%. The shot-to-shot variation of K-shell power was +/- 10% and for total power it was +/- 20%. In the interest of clarity only the result for shot Z2560 is shown. Z2560 was the highest yield shot with 363 kJ of K-shell emission. While circuit *A* gave a slightly smaller value for K-shell yield (327 kJ), the result for circuit *B* is significantly larger (445 kJ) than the Z2560 data. Also the K-shell pulse shape from circuit *A* matches the observed data much better than circuit *B*.

The time dependence of the total radiative power near the time of peak K-shell emission is shown in Fig. 5. Again, circuit *A* well represents this radiative property. Most interesting is that the peak power is ~ 40 TW of which ~ 30 TW is from the K-shell. This large a fraction of peak total power emitted from the K-shell observed in these argon gas-puff experiments is not typical for wire-array experiments. Even for a low Z experiment using an aluminum wire-array, where one might expect a higher fraction of the total radiative peak power to come from the K-shell because of the correspondingly lower K-shell ionization energy, this fraction is less than ~ 40 percent. For example, the peak K-shell power from high power aluminum shot Z1907 was 34 TW while its total peak radiative power was ~ 160 TW [18]. One of the highest aluminum K-shell yield experiments Z1974 had a K-yield of ~360 kJ [18] (a yield which is comparable to the argon gas-puff yields discussed here), and it achieved a total peak power of ~ 60 TW [18] TW of which only 26 TW was from the K-shell .

Overall circuit *A* is a better match to the data than circuit *B*, specifically for the K-shell continuum free-bound temperature, the total K-shell yield, the K-shell pulse shape, and the peak total radiative power. Before continuing with the analysis of results from circuit *A* we note a feature that may be useful for diagnosing the actual circuit behavior. Figure 6 shows the predicted K-shell yield as a function of load mass under the assumptions of circuit *A* and *B* electrical properties. The reason for showing this figure is to illustrate that larger K-shell yields may be attainable at higher mass loads than the experimental 1 mg/cm load mass, as long as downstream current losses are absent, as in circuit *B*. However, it is not assured that the current-loss circuit *A* parameters that were appropriate for the 1 mg/cm experiments will adequately represent the current flow into a more massive load. By benchmarking circuit parameters to a more massive load experiment, one may be able to determine the sensitivity of the circuit parameters to load mass, learn more about the nature of the current losses, and aid the construction of a more

predictive equivalent circuit model that is applicable to more than one load mass.

Given that the circuit *A* simulation reasonably represents the electrical and radiative properties of the experiments, it is worth examining the simulated plasma parameters for model *A* near the time of peak K-shell emission and comparing with other data taken for the Ar shots. In the experiments, Ar K-shell powers were diagnosed with photoconducting detectors (PCDs) which viewed the pinch region over Z=2.5-12.5 mm axial height through an aperture (where the cathode is at Z=0). This aperture avoided viewing the upper half of the pinch which was partially obscured by anode grid wires due to the 12 degree viewing angle of the PCDs. Uncertainty of ±10% in K-shell power was obtained by normalizing the PCD pulse shape to the weighted average K-shell yield measured by four independent diagnostics [1]. Figure 7 shows the thermal ion temperature, electron temperature, and electron density as a function of time during stagnation. At each time these simulated values have been averaged over the lower half of the pinch (z < 1.5 cm) and weighted by the local K-shell power. Thus they are representative of the properties in this restricted K-shell emitting part of the plasma. The rapid rise in the thermal ion temperature between -10 and -9 ns represents stagnation of the motional kinetic energy near the axis. Its subsequent decay results from equilibration with the electrons, which eventually occurs late in stagnation. However the electron temperature does not rise significantly because collisional excitation leads to the radiative losses, which is the objective of a plasma radiation source. The electron density also rises as stagnation proceeds. This is due to compression rather than ionization: one can see from the curve of the mean charge state that the plasma already begins at -10 ns in the He-like stage and gets ionized through the H-like state during stagnation. The increase in ion and electron density also accounts for the faster equilibration between ions and electrons as t > 0.

While the averaging used in Fig.7 to obtain time varying, spatially integrated quantities facilitates a discussion of the processes during stagnation, the simulated pinch is dynamic and spatially non-uniform as is illustrated in Fig. 8. This shows the K-shell emitted at a position (r, z) that escapes the whole plasma at several times throughout stagnation. These values are smaller than the locally emitted K-shell power because some of the radiation is absorbed in other parts of the plasma and that component is not included in the figure. The observed radius of the K-shell emitting plasma is 0.15 cm [1] and this extent reasonably agrees with that of the brightest calculated K-shell emitting regions noted on the Fig. 8 panel at t = 0 ns. The most intense K-shell emitting region in this simulation is located on the pinch axis and near the cathode side of the diode, between 0.5 cm and 1.0 cm.

The radiative powers in the Ar Ly-α, He-α, and He-α intercombination (IC) lines were included as part of the TCRE table output information so that the power in these lines could be calculated in the simulations. The experimental ratio of Ly-α/(He-α + IC) power is compared to the calculated ratio as a function of time in Fig. 9. The experimental line ratio shown in red is a composite of all three shots, which produced nearly identical ratios [1]. Figure 9 shows that the calculated and

experimental line ratio are in good agreement after the peak in the K-shell power, but prior to this time, the calculated ratio is considerably higher than that of the experiments, indicating higher temperatures in the simulated plasma early in the stagnation. One also sees in this figure that the line ratio peaks several ns before the peak of the K-shell power (t = 0). In the experimental data, however, the line ratio and K-shell power reach a maximum simultaneously. This difference in timing of the peak of the line ratio may be due to 3D effects [19] and [20] that we are unable to model with our 2D code, and it is also possible that it is due to time dependent ionization effects, which we discuss in a later section.

Experimental Ar Ly-β/(He-β + IC) and Ly-γ/He-γ line ratios were also determined near the time of peak K-shell power and they are discussed in reference [1]. While, these same line ratios can theoretically be calculated in a Mach2-TCRE simulation they are not compared with experiment for the following reason: For the hydrogen like ionization stage, the escape probability of the dominant radiating H-like line upon which the TCRE tables are based require radiation transport of only the J=3/2 component of the Ar Ly-α radiation. The radiative powers from the other higher level transitions of H-like argon are given by that of a uniform plasma that has the same ion density, same specific internal energy, and same P_{esc} in the J=3/2 component of the Ar Ly-α radiation. Likewise, the Ar He-like line powers are all based on the radiation transport of the J=1 component of the He-α line. Since the Ar Ly-α and He-α radiation account for the majority of the K-shell line radiation, this is a reasonable approximation.

IV. NON-LTE RADIATION PHYSICS

In this section we discuss three aspects of non-LTE physics relevant to z-pinch plasma radiation sources: non-local absorption of line emission, time dependent ionization kinetics, and the impact of flow velocity on line emission.

In section II.A. we described two different implementations of the probability-of-escape formalism. In the OTS approximation line absorption is accounted for through the whole plasma, but any absorption is applied to lowering emission rates in the emitting cell. For the in-line application of this approximation the probability-of-escape of a given emission line along each ray can be calculated using the optical depth from the emitting cell to the plasma edge. In the implementation using (1) any absorption along a ray through a cell is accumulated in that cell. So this non-local absorption is deposited in the absorbing cell and impacts the population kinetics in that cell. Consequently the formulae in [6] and [7] must be applied to cells along each ray for each transported line. We will refer to this second implementation as non-local deposition (NLD). Running this improved Mach2-TCRE model extends the computation time by a factor of ~ 4 over an OTS calculation. A 2DRMHD comparison between simulations performed with the formula (1) calculation for P_{esc} and the OTS approximation for P_{esc} has never been published. Figure 10 contains the total and K-shell power pulses from circuit model A. These are the same curves shown earlier and were calculated using NLD. The dashed lines in the this

figure show the total and K-shell pulses calculated using the OTS approximation. The circuit parameters are the same as that of A. The lower peak radiative powers at the time of peak K-shell emission exhibited by the OTS calculation is likely a consequence of the OTS model's overestimation of the emissivities at the center of the pinch and underestimation of the emissivities nearer the edge of the plasma, see Hansen *et al.* [21]. The K-shell yield for the OTS simulation was 346 kJ which is nearly the same as the 327 KJ yield obtained with the NLD model for P_{esc}, but the pulse shape is broader and accounts for the lower peak power value.

In the last section it was noted that calculated Ly-α/(He-α + IC) line ratio peaks at a larger value and earlier than in the experiments (see Fig.9). This may be attributable to an excessive electron temperature compared to the experiments. Another explanation is the implicit assumption of equilibrium, i.e., steady state, through use of our TCRE table. Because of this assumption the plasma ionizes instantaneously to its steady state value as the temperature and/or the electron density increases. Consider Fig.7. At -10 ns the electron temperature is ~1 keV and the Ar is primarily in the He-like stage. At this temperature the He- to H-like collisional ionization rate coefficient is ~1.3×10^{-13} cm^3/s. For the electron density of ~1×10^{20} cm^{-3} at this time, the ionization time scale would be about 80 ns, far larger than the 10 ns to peak power. In actuality as the plasma compresses and heats the ionization time would decrease, and explains the good agreement with experiment in Fig.9 after peak emission when the electron density is large according to Fig.7. This simple estimate shows that time dependent ionization could lead to a delay in the ionization process and, consequently a lower Ly-α/(He-α + IC) line ratio. Inclusion of time dependence in the population kinetics is not possible in the present tabular CRE methodology and is reserved for a future development.

Our simulations of the Ar pinches show significant velocity gradients near the axis at the time of stagnation, gradients sufficiently large enough to Doppler shift the emission from line centers into the wings. The radiation transport to account for Doppler shifts has not been fully implemented into an in-line treatment within Mach2-TCRE. Instead we post-process the simulation results to examine some of the impact of Doppler shifts on synthetic spectra.

The 2DRMHD simulations provided at each time dump the computational grid and, for each cell, the thermal ion and electron temperatures, radial velocity, and populations of the upper and lower states of each radiation line of interest. Consider a set of parallel rays perpendicular to the z-axis that cover the entire computational grid. Along each ray solve the radiative transfer equation using a frequency grid that covers a chosen radiative transition and is sufficiently dense to resolve Doppler shifts of a few km/s. Since the populations are known from the simulations one can readily calculate the emissivity and absorptivity at each frequency. In each cell the vector velocity is projected onto the ray and the line profile of the emissivity and absorptivity are Doppler shifted from the at-rest line center. The resulting intensities are a function of frequency (ν), displacement from the z-axis (y), axial position (z), and time, hence I(ν,y,z,t). If the intensities are integrated in z, then one has a temporally and radially resolved synthetic

spectrum, I(ν,y,t). If one further integrates in y then one has a temporally resolved spectrum, I(ν,t).

Figure 11 shows the He-α and intercombination line (IC) synthetic spectra integrated over y and z at +0.5 ns relative to peak power. To examine the impact of Doppler shifts, the above described transport is performed with and without the Doppler shifts. It is clear from this comparison that the large radial velocity gradients present in this circuit *A* simulation of the experiments are sufficient to significantly alter the intensity profile. In the no-Doppler case there are self absorption features at line center, especially for the resonance line. This absorption indicates that the emitting region is surrounded by a cooler region with a significant population of ground state He and little excitation. When the Doppler shifts are included the self absorption is diminished. Other impacts of the Doppler shifts are a broader profile because of the velocity shifted line energies, and a blue shift in the J=1 component of the Doppler modeled He-α emission.

By integrating the Doppler modeled emission in only the axial direction, the time-, radial-, and energy resolved synthetic spectra were generated for circuit *A* and the results are shown in Fig. 12 for -10 ns, -5 ns, 0 ns (time of peak K-shell power), and +5 ns after peak power. Two main points of interest illustrated by this figure are that there is a significant blue shift in the Ly-α emission 5 ns prior to the time of peak K-shell power. And at t=0 ns, the extent of the K-shell emission region is ~ 4 mm in diameter, which is close to that observed in the experiments (~3 mm).

At this time we cannot compare the calculated time-, radius- and energy resolved synthetic spectra with measured spectra because there is insufficient optically thin argon K-shell line information to absolutely calibrate the dispersion in the experiments (optically thin lines are needed to insure that there is no shift in the line center energy due to Doppler motion). Future experiments that contain a dopant such as chlorine would provide enough additional optically thin K-line energy information to make this calibration and comparison possible. For now, it is worth mentioning that in an earlier stainless steel experiment Z1861 (2.5 mg, 2 cm length, 65 mm diameter, 2:1 double wire array) [22] it was possible to unambiguously determine the spectral dispersion for the data since stainless steel naturally has Cr and Ni in addition to Fe. The low abundance of Cr and Ni means they act as dopants and their emission is optically thin. Iron, nickel, and chromium lines (Fe He-γ, Cr He-IC, Cr He-α, Cr He-γ, Ni He-IC, and Ni He-α) were used to calibrate the dispersion of the time-resolved elliptical crystal (TREX) spectrometer [23] and identify the spectral location of the line center energy for the Fe He-alpha and Fe- He IC emission, see Fig. 13. This figure shows, like our synthetic argon spectra, substantial blue shifts in He-α emission near the time of peak K-shell power. In our argon calculations this shift is due to large velocity gradients and we contend that a similar Doppler effect is producing the energy shifts in the stainless steel experiments.

V. CONCLUSION

We have benchmarked our 2DRMHD model against three recent argon experiments (same initial conditions – 8 cm diameter nozzle, 1 mg/cm, 2.5 cm length) performed on Sandia National Laboratories Z machine. By matching to both electrical properties of the machine and radiative properties of the experimental pinches, it was possible to determine current-loss circuit parameters that fit the experimental conditions. This circuit modeling demonstrates that it is likely that there were significant current losses downstream of the post-hole convolute. It also indicates that it would be worthwhile to perform an experiment at larger mass than 1 mg/cm. Such an experiment has the potential to produce more K-shell emission, and would allow us to both better understand the nature of the current losses as well as to determine the sensitivity of the circuit parameters to load mass.

Our "best" simulation was able to reproduce experimental: K-shell powers, K-shell yields, total powers, percentage of total K-shell emission emitted as line radiation, average electron temperature during the radiation pulse, and size of the K-shell emission region. Encouraged by this good match between experiment and simulation we inferred the experimental plasma temperatures and densities during the time of peak K-shell emission.

For the first time, we implemented an improved treatment of radiation transport in our 2DRMHD simulation model. In the past we relied on the "on-the-spot" approximation which means that we had only to calculate the absorption of photons along a trajectory out of the plasma. Here, we self-consistently model both absorption and emission of photons into and out of a computational plasma zone.

Using a post-process radiation transport model that includes Doppler effects we generated synthetic time-, space-, and energy-resolved spectra near the time of peak K-shell emission. The Doppler analysis of the simulated plasma conditions show that the velocity gradients are sufficient to produce broadened line profiles, spectral energy shifts and diminished line center absorption effects. The latter would otherwise be apparent in the absence of Doppler motion.

The simulated time-, space-, and energy resolved features for argon are similar to those present in stainless steel experiments performed on Z, In the future with a seeded argon plasma, e.g. a chlorine dopant, there should be enough additional optically line information to be able to calibrate the dispersion for the experimental K-shell spectra. At that time we can compare our synthetic spectra directly with the argon experimental results to infer implosion velocities near the time of stagnation.

ACKNOWLEDGMENT

REFERENCES

[1] B. Jones, J. P. Apruzese, A. J. Harvey-Thompson, D. J. Ampleford, C. A. Jennings, S. B. Hansen, N. W. Moore, D. C. Lamppa, D. Johnson, M. C. Jones, E. M. Waisman, C. A. Coverdale, M. E. Cuneo, G. A. Rochau, J. L. Giuliani, J. W. Thornhill, N. D. Ouart, Y. K. Chong, A. L. Velikovich, A. Dasgupta, M. Krishnan, and P. L. Coleman, "Effect of gradients at stagnation on K-shell X-ray yield in reproducible, high-current, fast Ar gas puff implosions," submitted to *Phys. Rev. Lett*

[2] H. Sze, J. Banister, P. L. Coleman, B. H. Failor, A. Fisher, J. S. Levine, Y. Song, E. M. Waisman, J. P. Apruzese, R. W. Clark, J. Davis, D. Mosher, J. W. Thornhill, A. L. Velikovich, B. V. Weber, C. A. Coverdale, C. Deeney, T. Gilliland, J. McGurn, R. Spielman, K. Struve, W. Stygar, and D. Bell, "Efficient argon K-shell radiation from a z pinch at currents >15 MA," *Phys. Plasmas,* vol. 8, pp. 3135-3138, July 2001.

[3] J. W. Thornhill, J. P. Apruzese, J. Davis, R. W. Clark, A. L. Velikovich, J. L. Giuliani, Jr., Y. K. Chong, K. G. Whitney, C. Deeney, C. A. Coverdale, and F. L. Cochran, "An efficient tabulated collisional radiative equilibrium radiation transport model suitable for multidimensional hydrodynamics calculations," *Phys. Plasmas*, vol. 8, pp. 3480-3489, July 2001.

[4] R. E. Peterkin, Jr. M. H. Frese, and C. R. Sovinec, "Transport of magnetic flux in an arbitrary coordinate ALE code," *J. Comput. Phys.*, vol. 140, pp. 148-171, 1998.

[5] A. Dasgupta, J. Davis, R. W. Clark, J. W. Thornhill, J. L. Giuliani, K. G. Whitney, and Y. K. Chong, "Impact of Dielectronic Recombination on ionization dynamics and spectroscopy of z-pinch stainless steel plasma," in *Seventh Int. Conf. on Dense Z Pinches*, AIP Proceedings #1088, edited by D. A. Hammer, and B. R. Krusse, pp. 37-40, 2009.

[6] J. P. Apruzese, J. Davis, D. Duston, and K. G. Whitney, "Direct solution of the equation of transfer using frequency and angle averaged photon escape probabilities, with application to a multistage, multilevel aluminum plasma," *J. Quant, Spectrosc, Radiat, Transf.* vol. 23 pp 479-487, 1980.

[7] J. P. Apruzese, "Direct solution of the equation of transfer using frequency and angle averaged photon-escape probabilities for spherical and cylindrical geometries," *J. Quant. Spectrosc. Radiat. Trans.*, vol. 25, pp 419-425, 1981.

[8] J. P. Apruzese, "An analytic Voigt profile escape probability approximation," *J. Quant. Spectrosc. Radiat. Trans.,* vol. 34, pp 447-452, 1985.

[9] B. G. Carlson, *Tables of equal weight quadrature EQ_n over the unit sphere*, Los Alamos Laboratory report LA-4734, 1971.

[10] D. E. Osterbrock, *Astrophysics of Gaseous Nebulae*, SanFrancisco, CA; Freeman, 1974, p. 19.

[11] J. P. Apruzese and J. L. Giuliani, "Multi-dimensional radiation transport modeling axisymmetric Z pinches: Ray tracing compared to Monte Carlo solutions for a two-level atom," *J. Quant. Spectrosc. Radiat. Transf.* vol. 11, pp. 134-143, 2010.

[12] M. Krishnan, K. W. Elliott, R. E. Madden, P. L. Coleman, J. R. Thompson, A. Bixler, *et al.,* "Architecture, implemtation, and testing of a multiple-shell gas injection system for high current implosions on the Z accelerator," *Rev. Sci. Instrum.*, vol. 84, no. 6, pp. 063504-1 – 063504-2, Jun. 2013.

[13] P. L. Coleman, D. C. Lamppa, R. E. Madden, K. Wilson-Elliott, B. Jones, D. J. Ampleford, *et al.*, "Development and use of a two-dimensional interferometer to measure mass flow from a multi-shell Z-pinch gas puff," *Rev. Sci. Instrum.*, vol 83, no. 8, pp. 083116-1 – 083116-10, Aug. 2012.

[14] B. Jones, C. A. Jennings, D. C. Lamppa, S. B. Hansen, A. J. Harvey Thompson, D. J. Ampleford, M. E. Cuneo, T. Strizic, D. Johnson, M. C. Jones, N. W. Moore, T. M. Flanagan, J. L. McKenney, E. M. Waisman, C. A. Coverdale, M. Krishnan, P. L. Coleman, K. Wilson-Elliott, R. E. Madden, J. Thompson, A.Bixler, J. W. Thornhill, J. L. Giuliani, Y. K. Chong. A. L. Velikovich. A. Dasgupta, and J. P. Apruzese,"A renewed capability for gas puff science on Sandia's Z machine," *IEEE Trans. Plasma Sci.*, vol. 42, no. 5,pp. 1145-1151, May 2014.

[15] J. W. Thornhill, J. L. Giuliani, Y. K. Chong, A. L. Velikovich, A. Dasgupta, J. P. Apruzese, et al., "Two-dimensional radiation MHD modeling assessment of designs for argon gas puff distributions for future experiments on the refurbished Z machine," High Energy Density Phys., vol. 8, no. 3, pp. 197–208, Sep. 2012.

[16] T. C. Wagoner, W. A. Stygar, H. C. Ives, T. L. Gilliland, R. B. Spielman, M. F. Johnson, P. G. Reynolds, J. K. Moore, R. L. Mourning, D. L. Fehl, K. E. Androlewicz, J. E. Bailey, R. S. Broyles, T. A. Dinwoodie, G. L. Donovan, M. E. Dudley, K. D. Hahn, A. A. Kim, J. R. Lee, R. J. Leeper, G. T. Leifeste, J. A. Melville, J. A. Mills, L. P. Mix, W. B. S. Moore, B. P. Peyton, J. L. Porter, G. A. Rochau, G. E. Rochau, M. E. Savage, J. F. Seamen, J. D. Serrano, A. W. Sharpe, R. W. Shoup, J. S. Slopek, C. S. Speas, K. W. Struve, D. M. V. D. Valde, and R. M. Woodring, "Differential-output B-dot and D-dot monitors for current and voltage measurements on a 20-MA, 3-MV pulsed-power accelerator," *Phys. Rev. STAB* 11, 100401-1 – 100401-18, Oct. 2008.

[17] C. A. Jennings, J. P. Chittenden, M. E. Cuneo, W. A. Stygar, D. J. Ampleford, E. M. Waisman, M. Jones, M. E. Savage, K. R. LeChien, and T. C. Wagoner, "Circuit modeling for driving three-dimensional resistive MHD wire array Z-pinch calculations," *IEEE Trans. Plasma Sci.*, vol. 38, no. 4, pp. 669-679, Apr. 2010.

[18] D. J. Ampleford, S. B. Hansen, C. A. Jennings, B. Jones, C. A. Coverdale, A. J. Harvey-Thompson, G. A. Rachau, G. Dunham, N. W. Moore, E. C. Harding, M. E. Cuneo, Y. K. Chong, R. W. Clark, N. Ouart, J. W. Thornhill, J. Giuliani, and J. P. Apruzese,"Opacity and gradients in aluminum wire array z-pinch implosions of the Z pulsed power facility," *Phys. Plasmas*, vol. 21, pp. 031201-1 – 031201-8, Feb. 2014.

[19] C. A. Jennings, M. E. Cuneo, E. M. Waisman, D. B. Sinars, D. J. Ampleford, G. R. Bennett, W. A. Stygar, and J. P. Chittenden, "Simulations of the implosion and stagnation of compact wire arrays," *Phys. Plasmas,* vol. 17, pp. 092703-1 – 092703-16, Sept. 2010.

[20] Edmund P. Yu, A. L. Velikovich, and Y. Maron, " Application of one-dimensional stagnation solutions to three-dimensional simulation of compact wire in absence of radiation," *Phys. Plasmas,* vol. 21, pp. 082703-1 – 082703-22, Aug. 2014.

[21] S. B. Hansen, B. Jones, J. L. Giuliani, J. P. Apruzese, J. W. Thornhill, H. A. Scott, D. J. Ampleford, C. A. Jennings, C. A. Coverdale, M. E. Cuneo, G. A. Rochau, J. E. Bailey, A. Dasgupta, R. W. Clark, J. Davis, "Doppler effects on 3-D non-LTE radiation transport and emission spectra," *High Energy Density Phys.*, vol. 7, pp. 303-311, June 2011.

[22] D. J. Ampleford, C. A. Jennings, B. Jones, S. B. Hansen, M. E. Cuneo, C. A. Coverdale, M. C. Jones, T. M. Flanagan, M. Savage, W. A. Stygar, M. R. Lopez, J. P. Apruzese, J. W. Thornhill, J. L. Giuliani, and Y. Maron, "K-shell emission trends from 60 to 130 cm/ms stainless steel implosions," *Phys. Plasmas*, vol. 20, pp. 103116-1 – 103116-7, Oct. 2013.

[23] J. E. Bailey, G. A. Chandler, S. A. Slutz, I. Golovkin, P. W. Lake, J. J. MacFarlane, R. C. Mancini, T. J. Burris-Mog, G. Cooper, R. J. Leeper, T. A. Mehlhorn, T. C. Moore, T. J. Nash, D. S. Nielsen, C. L. Ruiz, D. G. Schroen, and W. A. Varnum, " Hot dense capsule-implosion cores produced by Z-pinch dynamic hohlraum radiation," *Phys. Rev. Lett.* ,vol. 92, pp. 085002 -1 – 085002-4, Feb. 2004.
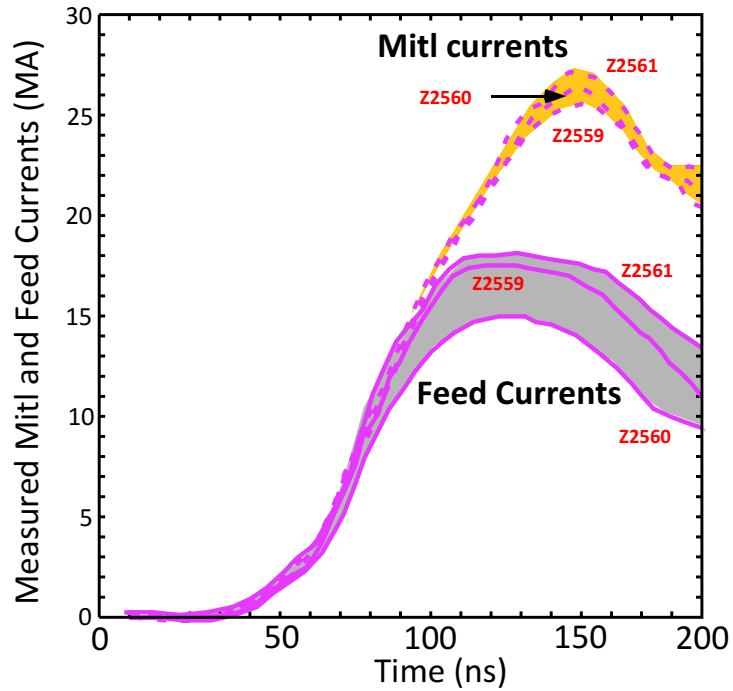
Fig. 1: Measured MITL and Feed currents of argon shots Z2559-61
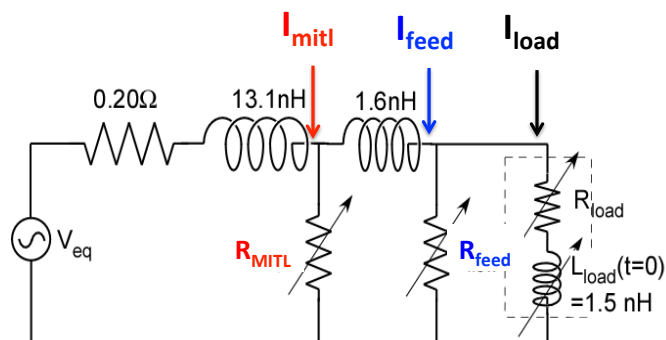
Fig. 2 Z machine equivalent circuit, V_{eq} is the open circuit voltage, I_{mitl} is the current measured in the MITL, I_{feed} is the current measured near the post-hole convolute, and I_{load} is the current flowing through the load (not measured). R_{fMITL} and R_{feed} are time dependent resistors that model MITL current losses and losses that occur in the feed region . R_{load} is the load resistance L_{load} is the load inductance.
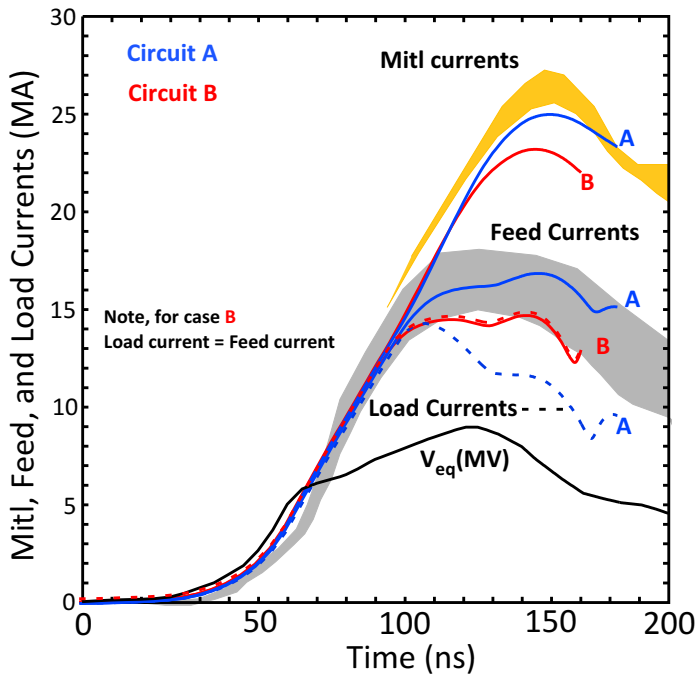
Fig. 3: MITL, Feed, and Load currents for circuit models *A* and *B*. The modeled drive voltage $V_{eq}(t)$ is also shown.
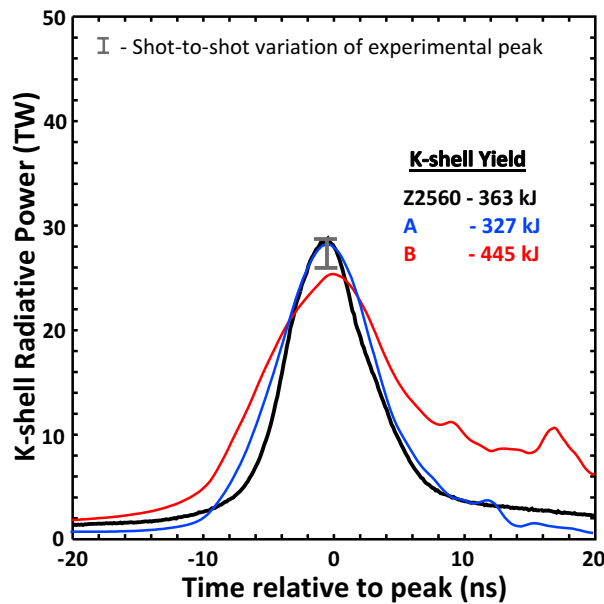
Fig. 4: K-shell radiative power and yields from circuit *A* and *B* simulations compared to experimental shot Z2560 results. The three experiment shot-to-shot variation of the peak power is also shown.
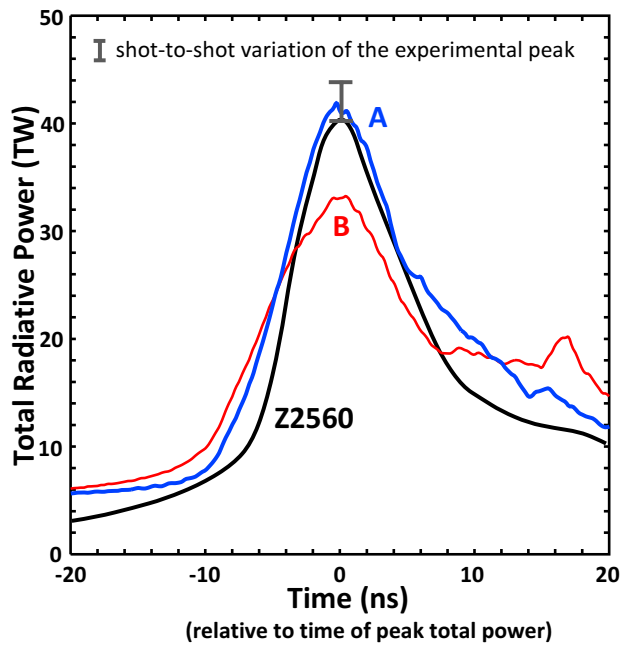
Fig. 5: Total Radiative power comparison between simulations *A* and *B* and experiment.
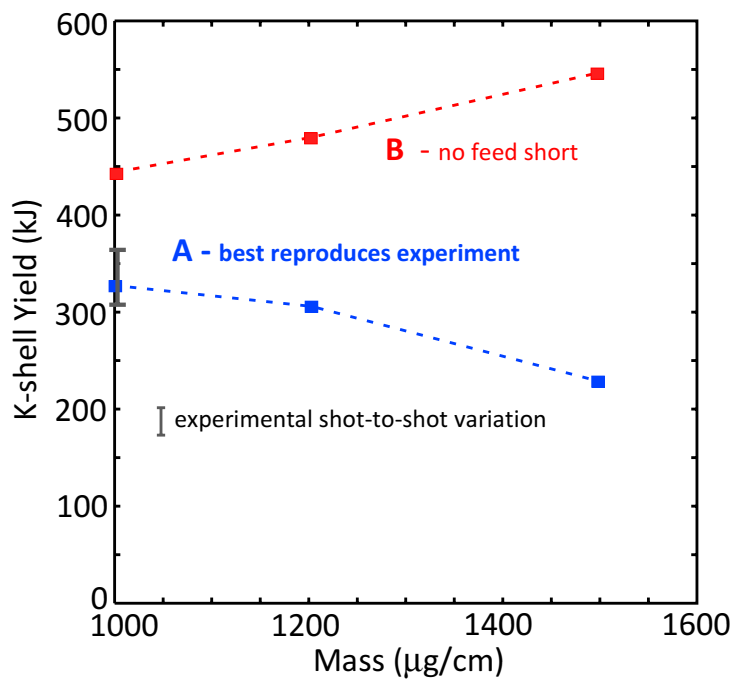
Fig. 6: K-shell yield versus load mass comparison between circuit *A* and *B* simulations.
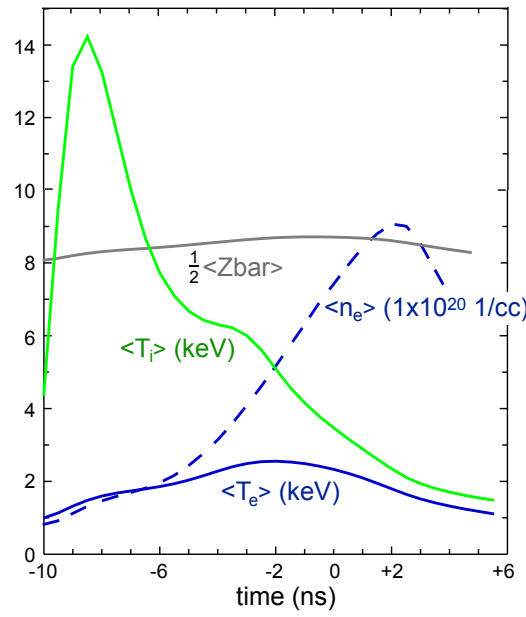
Fig. 7: K-shell power averaged $\langle T_i \rangle$, $\langle T_e \rangle$, $\langle Zbar \rangle$, and $\langle n_e \rangle$ near stagnation time for circuit *A* simulation.
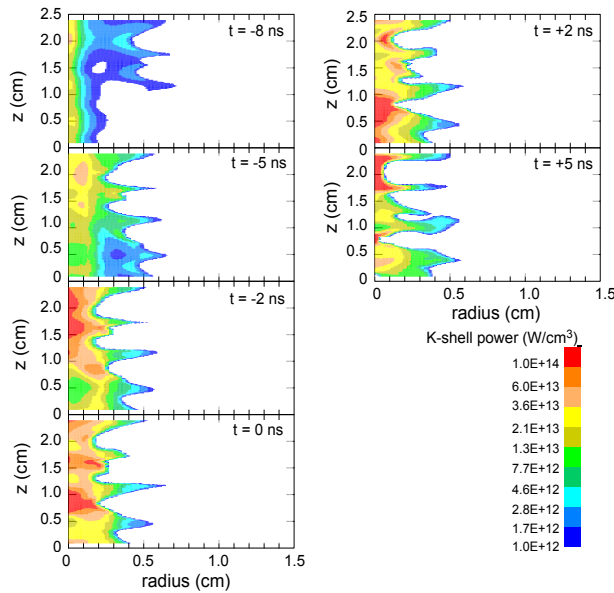
Fig. 8 K-shell power as a function of axial and radial position for times near peak K-shell power for the circuit *A* simulation.
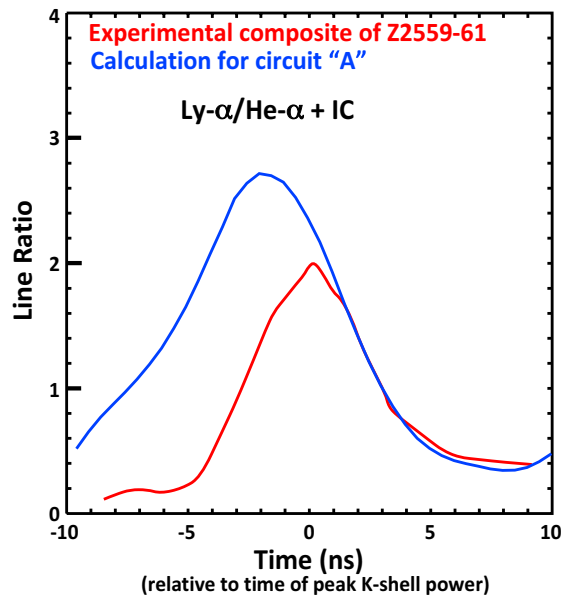
Fig. 9: Comparison of experimental and circuit *A* simulation results for Ly-α to He-α + IC line ratios near the time of peak K-shell power.
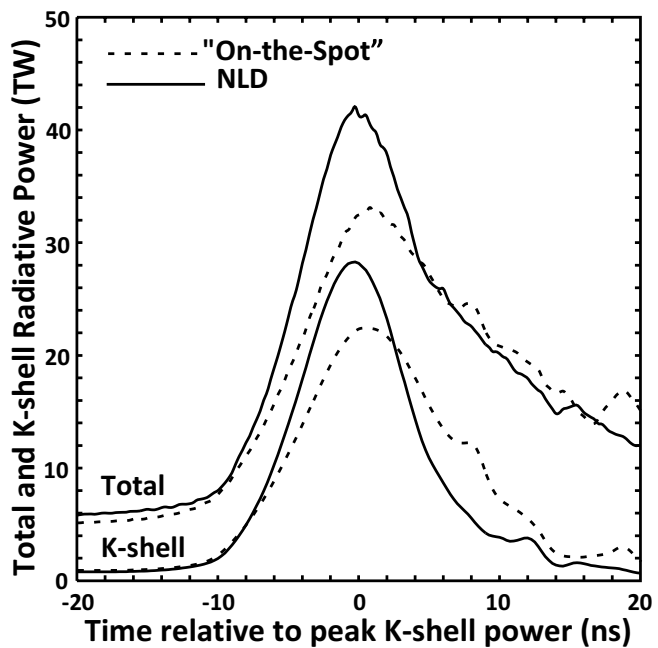

Fig. 10 Comparison of Total and K-shell radiative powers near the time of peak K-shell emission for simulations using the OTS and NLD models for P_{esc}.
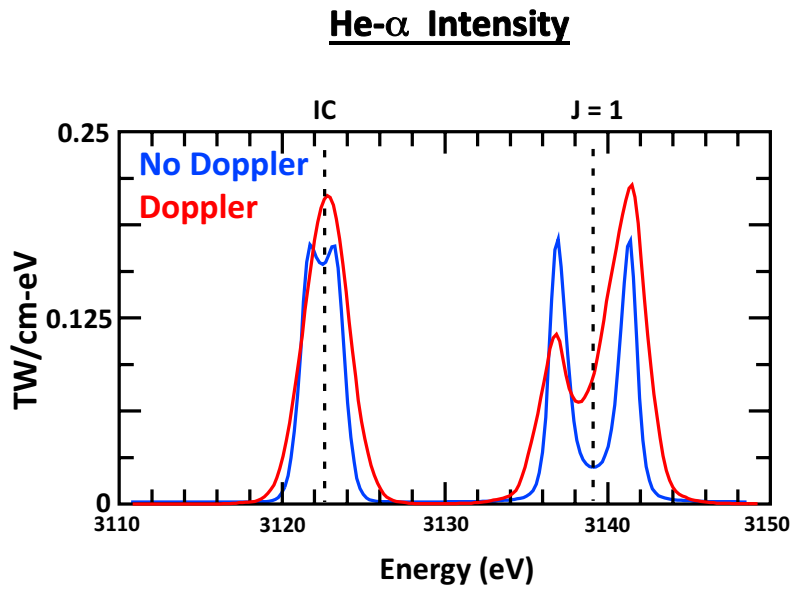
He-α Intensity

Fig. 11: Modeled He-α intensity at 0.5 ns after peak K-shell power for Circuit "*A*" simulation. Results are shown with and without Doppler effects.
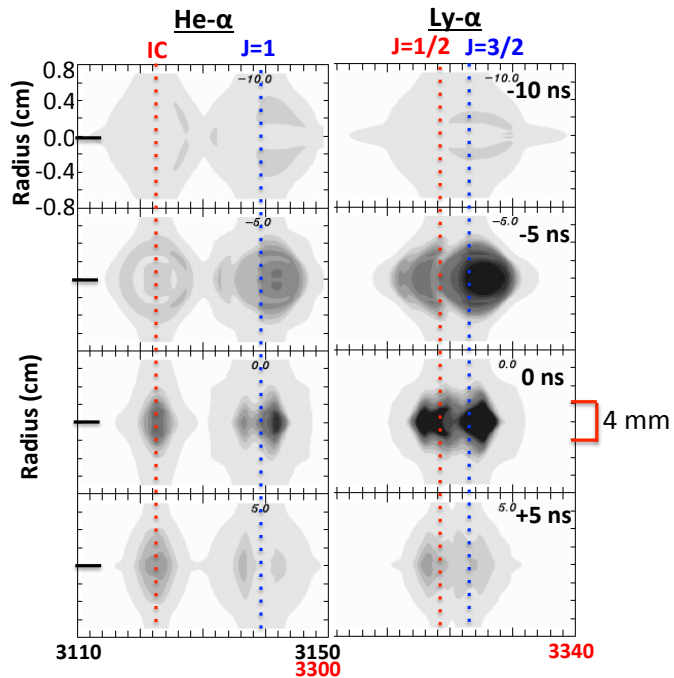

Fig. 12 Time-, space-, and energy-resolved synthetic spectra for circuit "*A*" simulation. Dashed lines represent line centers. 0 ns corresponds to the time of peak K-shell power
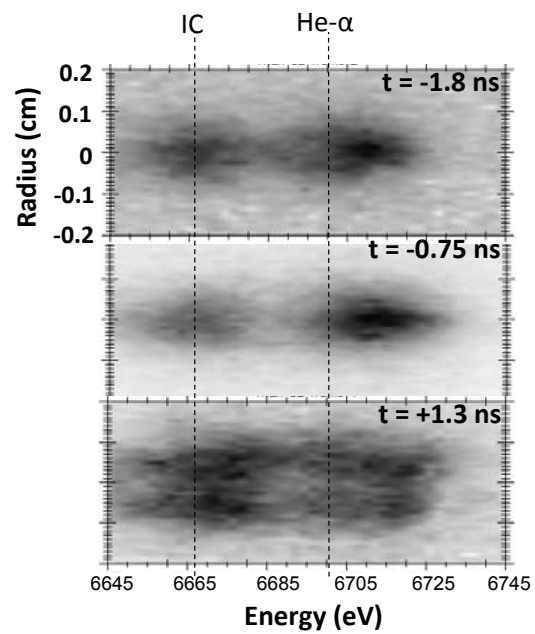
Fig. 13: Time-, radial-, and energy-resolved experimental spectra for stainless steel shot Z1861. Dashed lines are line centers.